XVIII International Conference on Water Resources
CMWR 2010
J. Carrera (Ed)

COMPUTATION OF FLUID CONFIGURATIONS AND CAPILLARY PRESSURES IN MIXED-WET 2D PORE SPACES FROM ROCK IMAGES

Johan O. Helland* **and Olav I. Frette†**

IRIS - International Research Institute of Stavanger
P.O. Box 8046, N-4068 Stavanger, Norway
e-mail: *johan.olav.helland@iris.no

Key words: Capillary pressure, arc meniscus, 2D pore geometry, mixed-wet rock

Summary. We present a model for capillary entry pressure and capillary pressure curve computations in mixed-wet 2D pore spaces from rock images. The model determines two curves defined by the loci of centre positions of two circles moving around the pore boundary in opposite directions. All relevant arc menisci are associated with intersections of these curves. At lines separating pore surfaces with different wettability, the circles rotate to permit pinned contact lines with associated hinging interfaces. Arc menisci and adjoining pore boundary segments are tracked to form boundaries of different regions. All possible combinations of these regions are generated and their associated entry pressure radii for invasion is computed by the Mayer & Stowe – Princen method, including thermodynamically consistent treatment of partial and complete displacement of oil layers forming at negative capillary pressure. It is demonstrated that the model captures well-known features of capillary behaviour at mixed-wet conditions. In particular, entry pressure radius, oil layer existence, fluid configurations and capillary pressure curves are strongly affected by the reversal point after drainage.

1 INTRODUCTION

Capillary pressure and wettability are key properties in the prediction of multiphase flow processes in porous rocks. Fluid distributions and capillary pressure curves are frequently calculated by pore-scale models, such as network models with idealized pore geometry [11], and more recently, by pore-morphology [3], level set [4] and lattice Boltzmann [5] models in realistic porous media. However, with these approaches it is difficult to incorporate a detailed wettability characterisation and to obtain accurate representations of the associated fluid configurations in the real pore geometry.

†Current address: Sintef Petroleum Research AS, Prof. Olav Hanssensvei 7A, N-4068 Stavanger, Norway. e-mail: olavinge.frette@sintef.no

The network model approach utilizes analytical capillary entry pressure solutions for piston-like invasion in straight idealised tubes, which are derived from the Mayer & Stowe – Princen (MS-P) method [6, 9]. In this method, the required work is balanced with the change in interfacial free energy for a virtual displacement of the invading main terminal meniscus (MTM) in the direction along the tube length. For a system of non-wetting and wetting phases, e.g., oil (o) and water (w), this balance may be written as

$$1/r = (dA_{os}\cos\theta + dA_{ow})/dV_o, \tag{1}$$

where dA_{os} and dA_{ow} are the changes in oil-solid and oil-water interfacial areas, respectively, dV_o is the change in oil volume, and θ is the contact angle. The radius of curvature, r, of an arc meniscus (AM) located in the tube cross-section sufficiently far away from the MTM is given by the Laplace formula in two dimensions

$$r = \sigma/p_c, \tag{2}$$

where σ is interfacial tension. Since capillary pressure p_c is assumed to be uniform everywhere, the entry pressure for a displacement of the MTM is related to the AM radius by Eq. (2). The MS-P method has been used to derive two- and three-phase capillary entry pressures in uniformly- and mixed-wet idealised pore geometries [9, 6, 7, 8]. The approach has recently been extended to allow computations in arbitrary, yet relatively convex, polygonal pore shapes by making use of the relation between the entry fluid configuration and the medial axis of the pore space [2, 10]. However, this latter extension is currently restricted to two-phase systems under conditions with zero contact angles.

We have developed a method to compute capillary entry pressures and fluid configurations in arbitrary, generally non-convex, uniformly-wet pore spaces from 2D rock images [1]. The present paper describes the extension of the model to mixed-wet conditions. This includes a method for computing thermodynamically consistent entry pressures for partial and complete oil layer displacements at negative capillary pressure [7].

2 PORE BOUNDARY AND WETTABILITY CHARACTERISATION

The novel model requires as input a 2D binary image of a simply connected pore space geometry. Our approach differs from [2] in that we calculate smooth pore boundaries from the image representations rather than constructing polygons with sharp corners. The main advantage of this approach is the possibility to compute curvature of the pore walls, which can be included in the augmented Young-Laplace equation to determine accurately the collapse of thin wetting films along the pore boundary during primary drainage [12]. This, in turn, could give an improved wettability characterisation with many adjacent pore wall segments of collapsed and intact films that require different advancing contact angles in subsequent imbibition processes.

We have implemented two options for obtaining smooth boundaries; a Euclidean path method which was adopted in [1], and a least squares method which is utilised in this

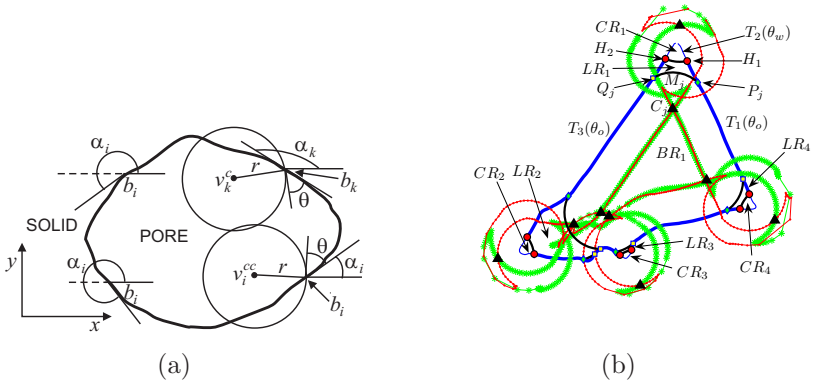

Figure 1: (a) Definition of the orientation angles α_i at pore boundary points b_i. The relation between the counter-clockwise and clockwise drainage curve points, v_i^{cc} and v_i^c, and the parameters θ, r and b_i are shown for uniform water-wet conditions. (b) Numerical example in a Bentheimer sandstone pore of the computation of v^c (green curve) and v^{cc} (red curve) for mixed-wet conditions. Oil-wet pore boundary segments $T_j(\theta_o)$ (bold blue lines), water-wet pore boundary segments $T_j(\theta_w)$ (thin blue lines), contact lines P_j ($\diamond$), Q_j ($\square$), pinning points H_j ($\circ$), relevant AMs M_j (black solid curves), relevant drainage curve intersections C_j ($\triangle$), and all CR, BR and LR regions are shown. The contact angles used are $\theta_o = 160°$ and $\theta_w = 20°$.

work. The computed smooth boundary of the pore space Ω is ordered in counter-clockwise direction and given by the set of points $\{b_i\}_{i=1}^N = \Gamma \subset \mathbb{R}^2$. For each b_i, we calculate an orientation angle $\alpha_i = \alpha(b_i)$ which is directed counter-clockwise from a line parallel with the x-axis, through the pore exterior (the solid phase), to the tangent of the pore boundary at b_i, as shown in Figure 1(a). The pore boundary is also organised in segments $\{T_j\}_{j=1}^{N_s}$ that are associated with uniform contact angles $\{\theta_j\}_{j=1}^{N_s}$. The endpoint of each segment equals the starting point of the next segment, i.e., $T_j \cap T_{j+1} = H_j$, where H_j are *pinning points* on the pore boundary where AMs may hinge during imbibition.

In this work mixed-wet conditions develop according to the scenario described in [12], by running our model for uniform wetting conditions [1] to an arbitrary interfacial curvature $1/r_{pd}$ which represents the end of primary drainage and an initial water saturation for imbibition. The segments T_j are assumed to connect adjoining contact lines of the AMs occurring at r_{pd}, and we restrict the present study to allow only two different contact angles along the pore boundary. If a segment T_j is in contact with oil, $\theta_j = \theta_o$, and if T_j is in contact with water, $\theta_j = \theta_w$.

3 MODEL DESCRIPTION

The method for computing entry pressure radii and associated fluid configurations takes as input an arbitrarily chosen radius $r \in [-r_{pd}, r_{pd}]$, which is related to capillary pressure by Eq. (2). The required steps of the algorithm for each r is described next.

3.1 Calculation of mixed-wet drainage curves

For uniform water-wet conditions, a circle with radius r is moved along the pore boundary such that its circular arc defines the given contact angle θ at each boundary point b. The circle movement is performed two times; in counter-clockwise and clockwise directions. In both cases the contact angle is defined at the front of the circle, see Figure 1(a). The resulting loci of circle centres, v^{cc} and v^{c}, constitute two closed curves that are referred to as the *counter-clockwise* and *clockwise drainage curves*. These are named after the concept *drainage axis* introduced by Lindquist [2]. To facilitate the calculation of these drainage curves at both positive and negative capillary pressures, we introduce the parameters $\bar{r}$ and $\bar{\theta}_\gamma, \gamma = o, w$ which are defined as

$$\bar{r} = \begin{cases} r & \text{if } r > 0, \\ -r & \text{if } r < 0, \end{cases} \quad \text{and} \quad \bar{\theta}_\gamma = \begin{cases} \theta_\gamma & \text{if } r > 0, \\ \pi - \theta_\gamma & \text{if } r < 0. \end{cases} \tag{3}$$

Then the drainage curves are calculated as follows for all $b_i = (x_i, y_i) \in T_j \setminus \{H_j, H_{j+1}\}$:

$$\begin{aligned} v_i^{cc} &= (x_i - \bar{r}\sin(\alpha_i + \bar{\theta}_j), y_i + \bar{r}\cos(\alpha_i + \bar{\theta}_j)), \\ v_i^{c} &= (x_i - \bar{r}\sin(\alpha_i - \bar{\theta}_j), y_i + \bar{r}\cos(\alpha_i - \bar{\theta}_j)), \end{aligned} \tag{4}$$

where $\bar{\theta}_j = \bar{\theta}_o$ or $\bar{\theta}_j = \bar{\theta}_w$. Note that these curves are generally different when $\bar{\theta}_j \neq 0$, but coincident when $\bar{\theta}_j = 0$. If the boundary point coincide with a pinning point, i.e., $b_i = H_j = T_j \cap T_{j+1}$, the drainage curves are constructed from Eq. (4) with $\bar{\theta}_j$ replaced by a sequence of m equally spaced values $\bar{\theta}_{H,j} = \{\bar{\theta}_j = \bar{\theta}_{h,1}, \ldots, \bar{\theta}_{h,m} = \bar{\theta}_{j+1}\}$. Thus, the circle with radius $\bar{r}$ is fixed at position b_i while it rotates from angle $\bar{\theta}_{h,1}$ until $\bar{\theta}_{h,m}$ is reached. The parameters $\bar{\theta}_h$ represent hinging angles which are required to model cases where contact lines are fixed at pinning points while the corresponding AMs hinge as capillary pressure changes [6]. Figure 2 illustrates the construction of these drainage curves on a flat surface with heterogeneous wettability for $r > 0$ and $r < 0$. The intersections of the two drainage curves constitute all the possible centre positions of circles whose arcs may correspond to physically allowed AMs for the given radius r.

3.2 Drainage curve intersections, contact lines and arc menisci

Each intersection C of the drainage curves is determined and associated with a contact line pair that coincide with boundary points b [1]. The so-called counter-clockwise contact line, $P \in \Gamma$, is associated with v^{cc}, and similarly, the clockwise contact line, $Q \in \Gamma$, is associated with v^{c}. The arc M, and its length L_M, of an intersection C is determined analytically by a set of generated arc points ordered from P to Q. For each M we also define pore boundary segments $S \in \Gamma$ which consists of the points tracked in counter-clockwise direction along the pore boundary from P to Q, i.e., $S = \{P = b_k, b_{k+1}, \ldots, b_{l-1}, b_l = Q\}$. A corresponding segment which excludes the contact lines is defined as $\widehat{S} = S \setminus \{P, Q\}$.

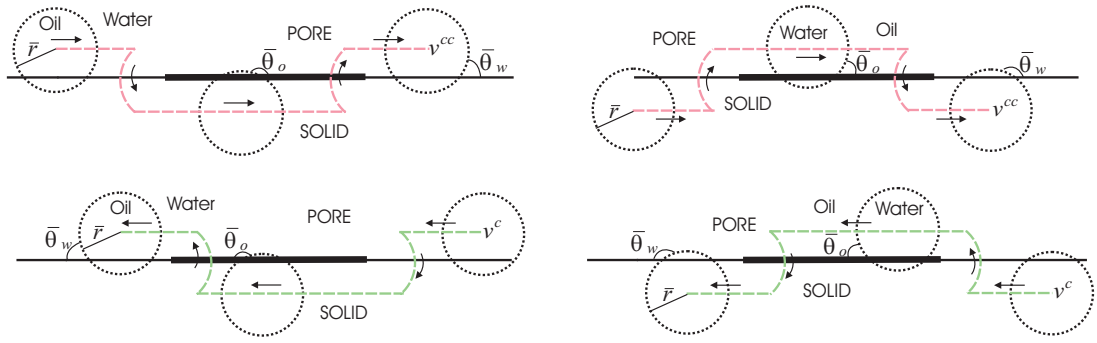

Figure 2: Illustration of the drainage curves v^{cc} and v^c on a flat surface with heterogeneous wettability for $r > 0$ (left) and $r < 0$ (right).

A set of criteria is implemented to identify the intersection points that correspond to geometrically meaningful AMs. For uniformly-wet conditions, this amounts in identifying all AMs pointing toward pore space constrictions [1]. For mixed-wet conditions, additional AMs pointing out of constrictions are geometrically allowed if the contact lines are pinned, i.e., $Q = H_k = T_k \cap T_{k+1}$ and $P = H_j = T_j \cap T_{j+1}$, and the contact angles satisfy $\bar{\theta}_j > \bar{\theta}_{j+1}, \bar{\theta}_{k+1} > \bar{\theta}_k$. The set of allowed AMs is denoted $\mathcal{M} = \mathcal{M}_T \cup \mathcal{M}_H$, where $\mathcal{M}_T$ represents AMs with contact lines located on uniformly-wet surfaces, and $\mathcal{M}_H$ represents AMs with contact lines located in pinning points. Figure 1(b) shows a rather simple Bentheimer sandstone pore with all allowed AMs for a radius $r < 0$ at mixed-wet conditions.

3.3 Extraction of geometrical regions

Geometrical regions in the pore space that correspond to fluid configurations are identified next. The closed boundary of such regions is formed by a sequence with alternating pore boundary segments and AMs. The algorithm makes use of the following definitions.

Definition 1. A *pore boundary segment*, $S_{i,j} \subset \Gamma$, is defined by a sequence of pore boundary points ordered in counter-clockwise direction, which connects two adjoining AMs M_i and M_j and includes their contact lines as segment endpoints. Its length, $L_{S,i,j}$, is the sum of the distances between all consecutive boundary points.

Definition 2. Two AMs, M_i and M_j, are *opposite* if $\widehat{S}_i \cup S_j = \Gamma$.

Definition 3. A *corner region*, CR, is a geometrical region defined for $r < 0$ with a boundary composed of segments $T_j(\theta_w)$ only and AMs $M_j \in \mathcal{M}_H$ of which none are opposite.

Definition 4. A *bulk region*, BR, is a geometrical region defined for all r with a boundary composed of segments $S_{i,j}$ and AMs $M_j \in \mathcal{M}$. Opposite AMs can only exist for $r < 0$ and must hinge, i.e., $M_j \in \mathcal{M}_H$, and also be part of the boundary of CR regions.

Definition 5. A *layer region*, LR, is a geometrical region defined for all r with a boundary composed of segments $S_{i,j}$ and at least two opposite AMs, $M_i, M_j \in \mathcal{M}$, of which at least one must be a member of $\mathcal{M}_T$.

A pore boundary tracking procedure is utilised to determine the different geometrical regions and closed boundaries [1]. The geometrical regions are classified according to Definitions 3–5 subsequently. Figure 1(b) indicates the different geometrical regions in a Bentheimer sandstone pore space for $r < 0$ at mixed-wet conditions.

3.4 Entry pressure radii for merged and individual regions

The valid fluid configuration change is associated with the most favourable entry pressure radius among all geometrically possible displacement scenarios [8]. Therefore, all geometrical regions existing at r are combined in all possible ways and evaluated by the MS-P method to determine the thermodynamically valid configuration. The considered invading fluid is oil for $r > 0$ and water for $r < 0$. All CR regions are assumed to be occupied by water. Invaded regions are organized in the set FR. Initially $FR = \emptyset$ for $r > 0$, and $FR = \{CR_j\}_{j=1}^{N_{CR}}$ for $r < 0$, where N_{CR} is the number of existing CR regions.

All regions which have not been invaded yet are evaluated to determine the favourable configuration change. This includes individual BR regions and combinations of BR and LR regions, which form larger *merged* regions K_i. Merged regions are determined by generating all possible combinations $K_{LR,i}$ of the LR regions and identifying the neighbouring BR regions for each combination, which together form larger regions K_i. If all the neighbouring regions of combination $K_{LR,i}$ is invaded, $K_i = K_{LR,i}$. The set $\mathcal{M}[K_i]$ represents all AMs that are part of K_i, excluding AMs separating internal neighbouring regions in K_i. The set of all segments $S_{j,k}$ that are part of K_i is given by $\mathcal{S}[K_i]$. For each K_i, we determine $\mathcal{M}_{F,i}$, representing AMs that separate K_i from already invaded neighbouring regions, and $\mathcal{M}_{E,i} = \mathcal{M}[K_i] \setminus \mathcal{M}_{F,i}$, representing AMs that separate K_i from other regions which have not been invaded yet. The MS-P equation, Eq. (1) can now be expressed for K_i as

$$\frac{1}{r_i} = F_i(r) = \begin{cases} \frac{(L_{os}\cos\theta)_i - L^F_{ow,i} + L^E_{ow,i}}{A_{o,i}}, & \text{if } r > 0, \\ \frac{(L_{os}\cos\theta)_i + L^F_{ow,i} - L^E_{ow,i}}{A_{o,i}}, & \text{if } r < 0, \end{cases} \tag{5}$$

where

$$\begin{aligned} (L_{os}\cos\theta)_i &= \textstyle\sum_{S_{j,k}\in\mathcal{S}[K_i]} L_{S,j,k}\cos\theta(S_{j,k}), \\ L^F_{ow,i} = \textstyle\sum_{M_j\in\mathcal{M}_{F,i}} L_{M,j}, &\quad L^E_{ow,i} = \textstyle\sum_{M_j\in\mathcal{M}_{E,i}} L_{M,j}. \end{aligned} \tag{6}$$

Here, $\theta(S_{j,k}) = \theta_o$ always because $\theta(S_{j,k}) = \theta_w$ only occurs in water-filled CR regions. The area $A_{o,i}$ is easily calculated by identifying the boundary of the merged region, which consists of segments $S_{j,k} \in \mathcal{S}[K_i]$ and AMs $M_j \in \mathcal{M}_{E,i} \cup \mathcal{M}_{F,i}$. The AM lengths are splitted into $L^E_{ow,i}$ and $L^F_{ow,i}$ to model partial oil layer displacements at $r < 0$ [8] and partial water layer displacements at $r > 0$ [1].

The right-hand side of Eq. (5) is more easily determined for individual regions. In this case, K_i represents a BR region, and for $r > 0$, $\mathcal{M}_{F,i} = \emptyset$ and $\mathcal{M}_{E,i} = \mathcal{M}[K_i]$, whereas for $r < 0$, $\mathcal{M}_{F,i}$ includes the AMs in $\mathcal{M}_H$ that separate the BR region from CR regions only.

4 COMPUTATIONAL PROCEDURE

Entry radii r_{entry} are calculated by the iterative procedure

$$1/r_{iter+1} = \begin{cases} \min\{F_i(r_{iter}), i = 1, \ldots, N_{comb}\} & \text{if } r > 0, \\ \max\{F_i(r_{iter}), i = 1, \ldots, N_{comb}\} & \text{if } r < 0, \end{cases} \tag{7}$$

where N_{comb} is the number of configuration candidates. The formula $1/r = L\cos\theta_o/A$ is assumed for the initial value, where A and L are pore space area and perimeter. All steps in Section 3 are repeated for each radius. The converged value r_{entry} is translated from pixels to physical units afterwards for capillary entry pressure estimation by Eq. (2).

Interfacial curvature – saturation curves are computed by taking as input a sequence of radii $r \in [-r_{pd}, r_{pd}]$. For each radius, all steps in Section 3 are repeated and the most favourable displacement is determined by

$$F^*(r) = \begin{cases} \min\{F_i(r) : 1/r \geq F_i(r), i = 1, \ldots, N_{comb}\} & \text{if } r > 0, \\ \max\{F_i(r) : 1/r \leq F_i(r), i = 1, \ldots, N_{comb}\} & \text{if } r < 0. \end{cases} \tag{8}$$

If the right-hand side is empty, the algorithm proceeds with the next radius since no region combination has reached the required entry condition. However, if $F^*(r)$ is determined, an entry condition is reached, and the associated merged or individual region is invaded and added to the set of invaded regions FR. Then the fluid configuration in the pore space has changed, and new region combinations are generated by taking into account all previously invaded regions at the current radius. If a new $F^*(r)$ is determined from Eq. (8) based on the new combinations, the corresponding regions are invaded and added to FR. The loop continues until the right-hand side of Eq. (8) is empty, and the algorithm proceeds with the next radius.

5 NUMERICAL RESULTS

Mixed-wet entry radii and interfacial curvature – saturation curves are computed by the novel model in a set of individual Bentheimer sandstone pore spaces that are extracted from a 2D SEM image taken at 1.28μm resolution. Entry radii are computed in 20 pore space geometries at different contact angles θ_o and radii r_{pd} at the end of drainage. The model [1] is run to r_{pd} in primary drainage using a zero contact angle. Then wettability is characterised based on the initial fluid configuration, using $\theta_w = 0^\circ$ on segments T_j in contact with water, and θ_o on segments in contact with oil.

All entry radius curvatures are plotted in Figure 3 as a function of $L\cos\theta_o/A$ (to the left) and $L\cos\theta_C/A$ (to the right). Here, θ_C is Cassie's contact angle which is defined as

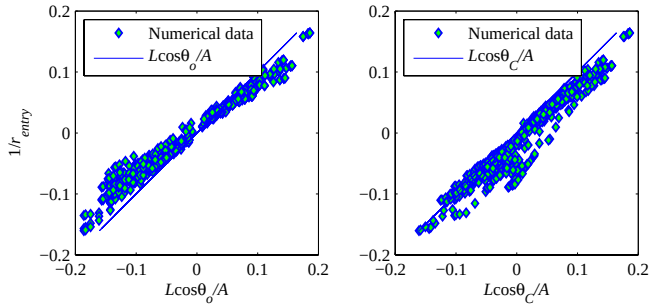

Figure 3: Computed entry radius curvatures in Bentheimer sandstone pore spaces plotted as a function of $L\cos\theta_o/A$ (left) and $L\cos\theta_C/A$ (right). Radii are determined in pixel units.

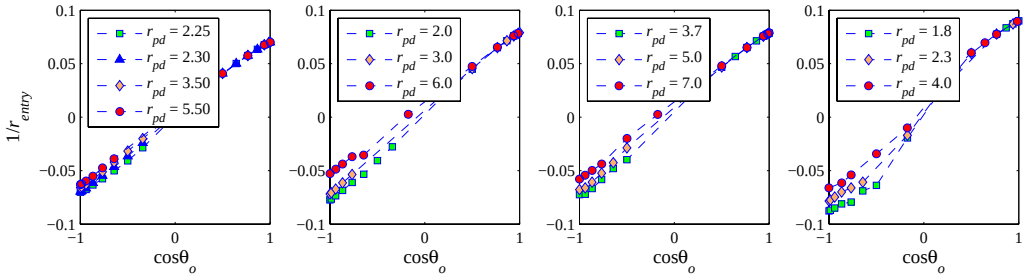

Figure 4: Computed entry radius curvatures in four Bentheimer sandstone pore spaces (from left to right) at different contact angles θ_o and r_{pd}. Radii are determined in pixel units.

$\cos\theta_C = (L_w\cos\theta_w + L_o\cos\theta_o)/L$, where L_w and L_o are the total lengths of all segments in contact with water and oil, respectively, at r_{pd}. The expression $L\cos\theta_o/A$ overestimates the computed entry radius curvatures, whereas $L\cos\theta_C/A$ captures the slope quite well, although the entry curvatures are generally overestimated for water-wet conditions and underestimated for oil-wet conditions. The latter trend is probably because the favourable entry curvatures depend less on the lengths of the water-wet boundary segments than what is reflected by θ_C, and hence the best approximated effective contact angle for these displacements can take larger values than θ_C.

Figure 4 shows $1/r_{entry}$ computations in four pore spaces as a function of θ_o at different r_{pd}. The effect of changing r_{pd} is most significant at oil-wet conditions. If $1/r_{pd}$ is small, the favourable invading region may share AMs with larger CR regions. The lengths of these AMs enter $L^F_{ow,i}$ in Eq. (5), which increases $1/r_{entry}$. For larger $1/r_{pd}$, the CR regions are smaller and the invading region may share AMs with residing oil layers instead. The lengths of these AMs enter $L^E_{ow,i}$ in Eq. (5), resulting in decreased $1/r_{entry}$. Figure 6 (left column) shows entry curvature configurations, which demonstrate that oil layers more likely form at strongly oil-wet conditions at large $1/r_{pd}$. Furthermore, the amount of oil

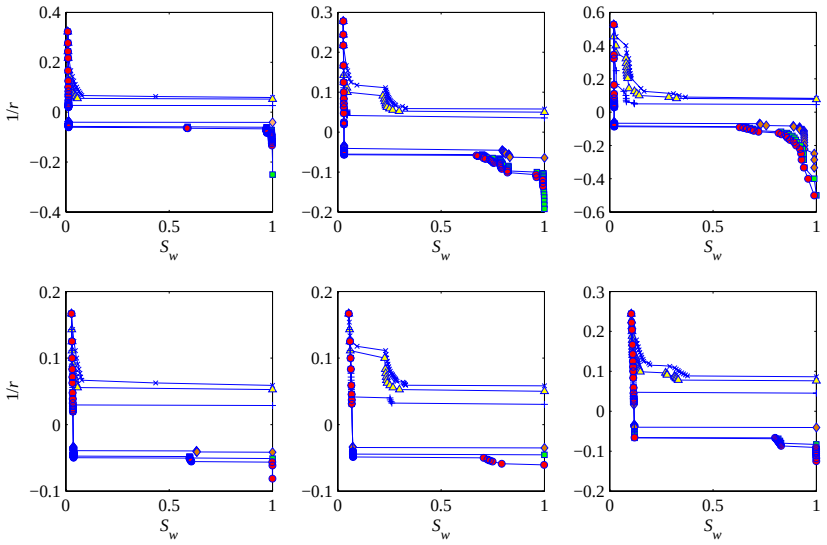

Figure 5: Interfacial curvature – saturation curves in three Bentheimer pore space geometries (column-wise) with small r_{pd} (top row) and large r_{pd} (bottom row), using $\theta_w = 0°$ and $\theta_o = 20°$ ($\times$), $\theta_o = 40°$ ($\triangle$), $\theta_o = 70°$ ($+$), $\theta_o = 130°$ ($\diamond$), $\theta_o = 160°$ ($\square$) and $\theta_o = 180°$ ($\circ$). Radii are determined in pixel units.

occupied in the pore after the most favourable region combination of water has invaded may be significant in strongly non-convex pore shapes.

Figure 5 presents mixed-wet interfacial curvature–saturation curves in three Bentheimer sandstone pore spaces for different θ_o and r_{pd}. These curves support our previous findings that r_{pd} may have a large impact on the entry pressure radii at oil-wet conditions. Moreover, in strongly non-convex pore spaces, several region combinations are invaded by water at curvatures smaller than the entry curvature reached first. This is also shown in the configurations plotted in Figure 6, where individual BR regions, merged LR and BR regions, and individual LR regions are invaded as the interfacial curvature decreases.

6 CONCLUSIONS

A novel model is developed for capillary entry pressure-, fluid configuration- and capillary pressure curve computations in mixed-wet 2D pore spaces with arbitrary shapes extracted from rock images. The model identifies all possible centre positions of circular arcs by moving two circles around the pore boundary in opposite directions. The loci of the circle centres constitute so-called counter-clockwise and clockwise drainage curves. All relevant arc menisci are associated with intersections of these curves. At lines separating pore surfaces with different wettability, the circles rotate to permit pinned contact lines with associated hinging interfaces. Arc menisci and adjoining pore boundary segments are tracked to form boundaries of different regions. All possible combinations of these

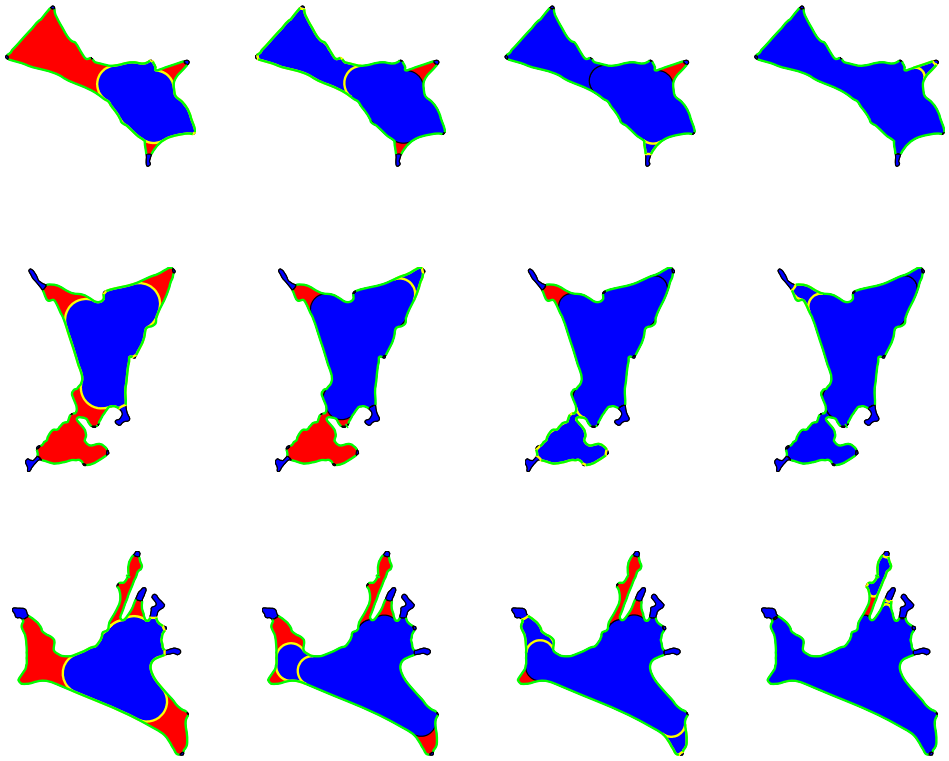

Figure 6: Evolution of mixed-wet fluid configurations as interfacial curvature decreases (from left to right) for the cases with small r_{pd} and $\theta_o = 180°$ presented in Figure 5 (top row). Water (blue), oil (red) and segments $T_j(\theta_o)$ (bold green lines) are highlighted. The yellow lines indicate the boundaries of new region combinations that are invaded by water at the current radius as determined by Eq. (8).

regions are generated and their associated entry pressure radii for invasion is computed by the Mayer & Stowe – Princen method, including thermodynamically consistent treatment of partial and complete displacement of oil layers forming at negative capillary pressure. It is demonstrated that the model captures well-known features of capillary behaviour at mixed-wet conditions. In particular, entry pressure radius, oil layer existence, fluid configurations and capillary pressure curves are strongly affected by the reversal point after drainage. Additional displacements occurring at interface curvatures below the first reached entry curvature is included in the model, and it is observed that displacements which involve several regions and partial displacement of oil layers occur frequently in strongly non-convex Bentheimer pore space geometries.

ACKNOWLEDGMENTS

Financial support was provided by the Research Council of Norway, ConocoPhillips and the Ekofisk co-venturers, including TOTAL, ENI, StatoilHydro and Petoro.

REFERENCES

[1] O.I. Frette and J.O. Helland. A semi-analytical model for computation of capillary entry pressures and fluid configurations in uniformly-wet pore spaces from 2D rock images. *Adv. Water Resour.*, doi:10.1016/j.advwatres.2010.05.002, (2010).

[2] W.B. Lindquist. The geometry of primary drainage. *J. Coll. Interf. Sci.*, **296**, 655-668, (2006).

[3] M. Hilpert and C.T. Miller. Pore-morphology-based simulation of drainage in totally wetting porous media. *Adv. Water Resour.*, **24**, 243–255, (2001).

[4] M. Prodanovic and S.L. Bryant. A level set method for determining critical curvatures for drainage and imbibition. *J. Coll. Interf. Sci.*, **304**, 442–458, (2006).

[5] M.G. Schaap, M.L. Porter, B.S.B. Christensen and D. Wildenschild. Comparison of pressure-saturation characteristics derived from computed tomography and lattice Boltzmann simulations. *Water Resour. Res.*, **43**, W12S06, doi:10.1029/2006WR005730, (2007).

[6] S. Ma, G. Mason and N.R. Morrow. Effect of contact angle on drainage and imbibition in regular polygonal tubes. *Coll. Surf. A: Phys. Eng. Asp.*, **117**, 273–291, (1996).

[7] M.I.J. van Dijke and K.S. Sorbie. Existence of fluid layers in the corners of a capillary with non-uniform wettability. *J. Coll. Interf. Sci.*, **293**(2), 455–463, (2006).

[8] M.I.J. van Dijke, M. Piri, J.O. Helland, K.S. Sorbie, M.J. Blunt and S.M. Skjæveland. Criteria for three-fluid configurations including layers in a pore with nonuniform wettability. *Water Resour. Res.*, **43**, W12S05, doi:10.1029/2006WR005761, (2007).

[9] M. lago and M. Araujo. Threshold pressure in capillaries with polygonal cross section. *J. Coll. Interf. Sci.*, **243**, 219–226, (2001).

[10] M. Held. Analytical computation of arc menisci configuration under primary drainage in convex capillary cross sections. *Comput. Geosci.*, **14**(2), 311–317, (2010).

[11] P.E. Øren, S. Bakke and O.J. Arntzen. Extending predictive capabilities to network models. *SPE Journal*, **3**, 324–336, (1998).

[12] A.R. Kovscek, H. Wong and C.J. Radke. A pore-level scenario for the development of mixed wettability in oil reservoirs. *Am. Inst. Chem. Eng. J.*, **39**, 1072–1085, (1993).